PAPER

Efficient polysulfide trapping in lithium–sulfur batteries using ultrathin and flexible BaTiO₃/graphene oxide/carbon nanotube layers†

Jing Wang,[a] Zhe Shi,[b] Yufeng Luo,[a] Datao Wang,[a] Hengcai Wu,[a] Qunqing Li,[a,c] Shoushan Fan,[a,c] Ju Li [ID][b] and Jiaping Wang [ID] *[a,c]

Ultrathin and flexible layers containing BaTiO₃ (BTO) nanoparticles, graphene oxide (GO) sheets, and carbon nanotube (CNT) films (BTO/GO@CNT) are used to trap solvated polysulfides and alleviate the shuttle effect in lithium–sulfur (Li–S) batteries. In the functional layers, the CNT films build a conductive framework, and the GO sheets form a support membrane for the uniform dispersion of BTO nanoparticles. BTO nanoparticles without ferroelectricity (nfBTO) can trap polysulfides more effectively by chemical interaction compared to BTO nanoparticles with ferroelectricity (fBTO). A Li–S cell with the nfBTO/GO@CNT functional layer exhibits a reversible capacity of 824.5 mA h g⁻¹ over 100 cycles at 0.2 C. At a high sulfur loading of 5.49 mg cm⁻², an electrode with the functional layer shows an areal capacity of 5.15 mA h cm⁻² at 0.1 C, demonstrating the nfBTO/GO@CNT functional layer's potential in developing high-performance Li–S batteries.

Introduction

Recently, the demand for high energy density batteries for use in electric vehicles and portable electronic devices has been increasing very rapidly. Among all the rechargeable batteries, the lithium–sulfur (Li–S) battery shows great potential due to its high theoretical capacity of 1675 mA h g⁻¹ and low material cost.[1,2] However, there exist several critical challenges for the practical applications of Li–S batteries. Both the active sulfur material and the discharge products have very low conductivity. During cycling, the volume change of the sulfur electrodes can be as high as 80%. Moreover, the intermediate polysulfides (Li_2S_n, $4 \leq n \leq 8$) tend to dissolve in the ether electrolyte, and the conventional separator cannot inhibit the shuttle of the polysulfides between cathodes and anodes.[3,4] All these issues give rise to active substance loss, rapid capacity decay, low coulombic efficiency, and inferior rate performances of Li–S batteries.

Carbonaceous materials, such as carbon nanotubes (CNTs) and graphene, and their composites, have been widely used as scaffolds in Li–S batteries.[5–12] Carbon materials can increase the conductivity of sulfur electrodes and their porous structure can accommodate the volume expansion of electrodes during cycling. However, carbon composites with nonpolar surfaces cannot trap polar polysulfides efficiently.[13,14] An alternative strategy is introducing polar metal-based compounds, such as metal oxides,[15–19] sulfides,[20–22] nitrides,[23–25] phosphides,[26,27] and carbides,[28,29] into the electrode or separator of Li–S batteries. These polar metal-based compounds can form solid chemical bonding with polysulfides and show a catalytic effect to promote the redox reactivity of polysulfides. However, most of the metal-based compounds have a higher density than sulfur, and the introduction of these compounds in sulfur electrodes might reduce the energy density of the electrodes. Moreover, it is difficult for the traditional porous and nonpolar polypropylene/polyethylene separator to restrain polysulfides. To solve these problems, functional layers containing carbon materials and a limited amount of polar metal-based compounds are coated on conventional separators to suppress the migration of polysulfides effectively.

Herein, an ultrathin and flexible layer containing BaTiO₃ (BTO) nanoparticles, graphene oxide (GO) sheets, and CNT films (BTO/GO@CNT) was used between the pristine separator and the sulfur electrode, aiming to trap solvated polysulfides and alleviate the shuttle effect in Li–S batteries. A cross-stacked CNT film was attached to the separator. GO sheets and BTO nanoparticles were ultra-sonicated and uniformly deposited on the CNT films. By repeating this process, a sandwiched BTO/GO@CNT layer was obtained (Fig. 1a and b). The CNT films built an ultrathin conductive network and provided

[a]Department of Physics and Tsinghua-Foxconn Nanotechnology Research Center, Tsinghua University, Beijing 100084, China. E-mail: jpwang@tsinghua.edu.cn
[b]Department of Nuclear Science and Engineering and Department of Materials Science and Engineering, Massachusetts Institute of Technology, Cambridge, MA 02139, USA
[c]Frontier Science Center for Quantum Information, Beijing 100084, China
†Electronic supplementary information (ESI) available. See DOI: 10.1039/d0nr08625h
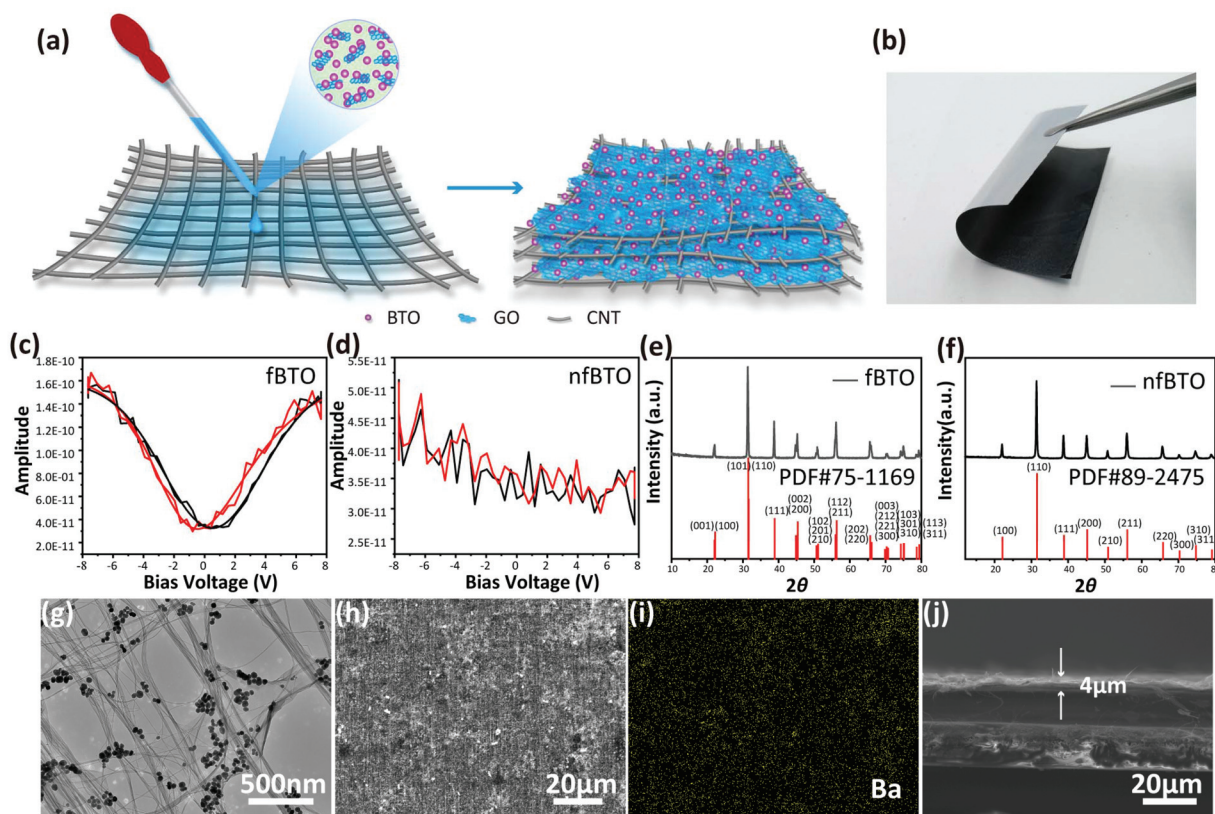
Fig. 1 (a) Schematic of the fabrication of a BTO/GO@CNT layer. (b) Photograph of a separator with a BTO/GO@CNT layer. Local PFM amplitude–bias voltage curves of (c) fBTO and (d) nfBTO particles. XRD patterns of (e) fBTO and (f) nfBTO particles. (g) TEM and (h) SEM images of an nfBTO/GO@CNT functional layer. (i) Ba elemental mapping of (h). (j) Cross-sectional SEM image of an nfBTO/GO@CNT functional layer.

ion pathways, thus reducing the Li–S cell's internal impedance. GO sheets served as support membranes for the uniform dispersion of BTO nanoparticles and hindered the diffusion of polysulfides. As one of the polar metal-based compounds, BTO nanoparticles with ferroelectricity (fBTO) have recently been applied in Li–S batteries.[30–33] By introducing the fBTO nanoparticles into Li–S batteries, the electrochemical performances were improved. The fBTO nanoparticles with ferroelectricity built an internal electric field that originated from spontaneous polarization. Polysulfides are heteropolar and can be anchored within the interlayer due to the electric field.[30] Therefore, ferroelectricity has an effect on the adsorption of polysulfides. In this work, BTO nanoparticles with ferroelectricity (fBTO) and without ferroelectricity (nfBTO) were used in the BTO/GO@CNT functional layer. Polysulfide adsorption tests and density functional theory (DFT) simulations demonstrated that the nfBTO nanoparticles exhibited a better ability to trap polysulfides by chemical reaction than fBTO nanoparticles. Electrochemical measurements verified that the nfBTO/GO@CNT functional layer effectively suppressed the polysulfide shuttle effect and enhanced the performances of Li–S batteries. The battery with the nfBTO/GO@CNT functional layer delivered an initial specific capacity of 1187.8 mA h g^{-1} at 0.1 C and showed a reversible capacity of 824.5 mA h g^{-1} over 100 cycles at 0.2 C.

Experimental

Fabrication of the BTO/GO@CNT layer

Super-aligned carbon nanotubes (SACNTs) were synthesized by chemical vapor deposition.[34–36] Continuous CNT films can be drawn from SACNT arrays by an end-to-end joining mechanism.[37–39] The BTO/GO suspension was obtained by dispersing BTO (nfBTO and fBTO) nanoparticles (analytical reagent, purity > 99.7%, Aladdin) and GO sheets in ethyl alcohol. The mixture was intensively ultra-sonicated for 30 min. After attaching the pristine separator to a glass plate, one layer of the CNT film was put on the separator. After rotating the glass plate 90 degrees, another layer of the CNT film was put on the top to build a cross-stacked CNT film on the separator. The BTO/GO suspension was dropped on the cross-stacked CNT films and it diffused uniformly in the CNT films, and ethyl alcohol quickly evaporated. The same procedure was repeated five times to obtain an ultrathin sandwich-structured BTO/GO@CNT layer. The areal densities of BTO nanoparticles and GO sheets were 0.15 mg cm^{-1} and 0.05 mg cm^{-1}, respectively. The BTO/GO@CNT layers were punched into disks (19 mm in diameter).

Fabrication of CNT@S electrodes

CNTs were heated at 550 °C in air for 30 min. Then 10 mg of CNTs was dispersed in 40 ml of mixed ethyl alcohol–water

solution at a volume ratio of 1 : 1 by ultra-sonication for 30 min. 20 mg of sulfur powder was dispersed in 30 ml of ethyl alcohol by ultrasonication for 30 min. The CNT suspension was added to the solvent of sulfur slowly to avoid self-aggregation of sulfur. The mixture solution was further sonicated for 30 min to obtain a homogeneous suspension. The CNT@S sheet was obtained by vacuum filtration. After drying at 45 °C, the composite electrode was heated in a sealed autoclave to 155 °C for 12 h. Finally, the CNT@S sheet was cut into disks of 10 mm diameter as electrodes.

Lithium polysulfide adsorption and trapping tests

Li_2S_4 solutions were obtained by adding Li_2S and S at a molar ratio of 1 : 3 in dioxolane/dimethoxyethane (DOL/DME, 1 : 1 by volume) under vigorous stirring at 60 °C for 24 h. H-type glass bottles were used in the polysulfide trapping test. The left and right glass bottles contain 0.033 M Li_2S_4 solution and the DOL/DME solvent, respectively. The pristine separator and the separators with the nfBTO/GO@CNT and fBTO/GO@CNT functional layers were put between the two glass bottles. The polysulfide adsorption test was performed by adding nfBTO nanoparticles and fBTO nanoparticles to 0.005 M Li_2S_4 solution.

Characterization

Thermogravimetric analysis (TGA) of the CNT@S electrode was performed in air (Netzsch STA 449 F3 Jupiter, 30–800 °C) to determine the sulfur content in the electrode. Transmission electron microscopy (TEM, Tecnai G2F20, FEI) and scanning electron microscopy (SEM, Sirion 200, FEI) were performed to observe the morphology of the BTO/GO@CNT functional layer. X-ray diffraction (XRD, Rigaku D/max-2500/PC) was performed to characterize the crystallinity of BTO nanoparticles. X-ray photoelectron spectroscopy (XPS, PHI Quantera II) analysis was performed to detect the BTO and sulfur interaction. UV-vis characterization was carried out on a spectrometer (PerkinElmer Lambda 950). Piezoresponse force microscopy (PFM) analysis was carried out on a scanning probe microscope (Asylum, MFP-3D-SA).

Electrochemical measurements

Coin-type and pouch cells were assembled in a glovebox (M. Braun) under an argon atmosphere. Circular CNT@S cathodes were used in coin-type cells. 2 cm × 2 cm CNT@S cathodes were used in pouch cells. The separators were coated by the BTO/GO@CNT layer, and lithium metal was used as the anode. 1 M LiTFSI solution in DOL/DME (1 : 1 by volume) with the addition of 0.2 M $LiNO_3$ was the electrolyte. Galvanostatic performances of the cells were characterized using a Land battery system, and the cutoff voltages were 1.6–2.8 V. Electrochemical impedance spectroscopy (EIS) and cyclic voltammetry (CV) measurements were performed using a galvanostat instrument (Bio-Logic VMP-3).

First-principles simulations

DFT calculations were employed to investigate the polysulfide adsorption ability of BTO (nfBTO and fBTO). For the simu-

lation of the adsorption of Li_2S_n on BTO, a slab of four BTO layers (the two bottom layers were frozen during the optimization) was built to model the BTO (001) surface, which was determined as the most frequently exposed surface in the experiment. In all cases, a vacuum spacing of 10 Å was maintained to prevent periodic interactions. The binding energy (E_b) was used to measure the adsorbing ability and could be determined as the difference between the total energy of the Li_2S_n-adsorbed system (E_{total}) and the sum of the energies of isolated Li_2S_n (E_{Li2Sn}) and a clean BTO substrate ($E_{substrate}$), *i.e.*, $E_b = E_{total} - (E_{Li2Sn} + E_{substrate})$. A larger difference suggests greater adsorbing ability. The Perdew–Burke–Ernzerhof methods[40,41] implemented in VASP[42] were used. The van der Waals interaction was included through DFT-D3.[43] To expand the electronic wave functions with a plane-wave basis set, a 400 eV energy cutoff was used. The Monkhorst–Pack[44] k-point mesh was $1 \times 1 \times 1$. The maximum residual force was maintained below 0.02 eV Å^{-1} for atomic relaxation.

Results and discussion

The ferroelectricity of two kinds of BTO nanoparticles was characterized by PFM. The hysteresis curves in Fig. 1c show that the fBTO nanoparticles deliver an intrinsic polarization due to their ferroelectricity. The curves for the nfBTO nanoparticles did not show any hysteresis loop due to non-ferroelectricity (Fig. 1d). The XRD spectra in Fig. 1e and f show phases and crystal structures of the BTO particles. The fBTO nanoparticles had a tetragonal *P4mm* structure with lattice parameters of a = 3.994 Å and c = 4.038 Å, an asymmetric crystal structure that possesses spontaneous polarization. The nfBTO possessed a cubic *Pm3̄m* structure with lattice parameters of a = 4.0177 Å and c = 4.0177 Å.

The morphology and structure of the BTO/GO@CNT layers were characterized by both SEM and TEM. The nfBTO/GO@CNT and fBTO/GO@CNT layers exhibited similar morphologies. The sizes of both nfBTO and fBTO particles were around 50–100 nm (Fig. 1g and S1a†). The GO sheets served as a support for the dispersion of the BTO nanoparticles and covered the pores in the CNT films. The CNT films built a conductive framework, and the BTO nanoparticles and the GO sheets were sandwiched within the CNT films. SEM images showed that the CNT films, GO sheets, and BTO nanoparticles covered the separator completely. The energy-dispersive X-ray (EDX) mapping showed that the Ba element was distributed uniformly, indicating a homogeneous dispersion of BTO particles on the layer (Fig. 1h, i and S1b, S1c†). The layer was ultrathin with a thickness of 4 μm (Fig. 1j).

The electrochemical performances of CNT@S electrodes containing the pristine separator and the nfBTO/GO@CNT and fBTO/GO@CNT functional layers were characterized using coin cells. The CNT@S electrodes demonstrated high flexibility, and the TGA result showed that the content of sulfur in the electrode was 64.27 wt% (Fig. S2†), corresponding to an areal density of 2.8 mg cm^{-2}. The cycle performances of the
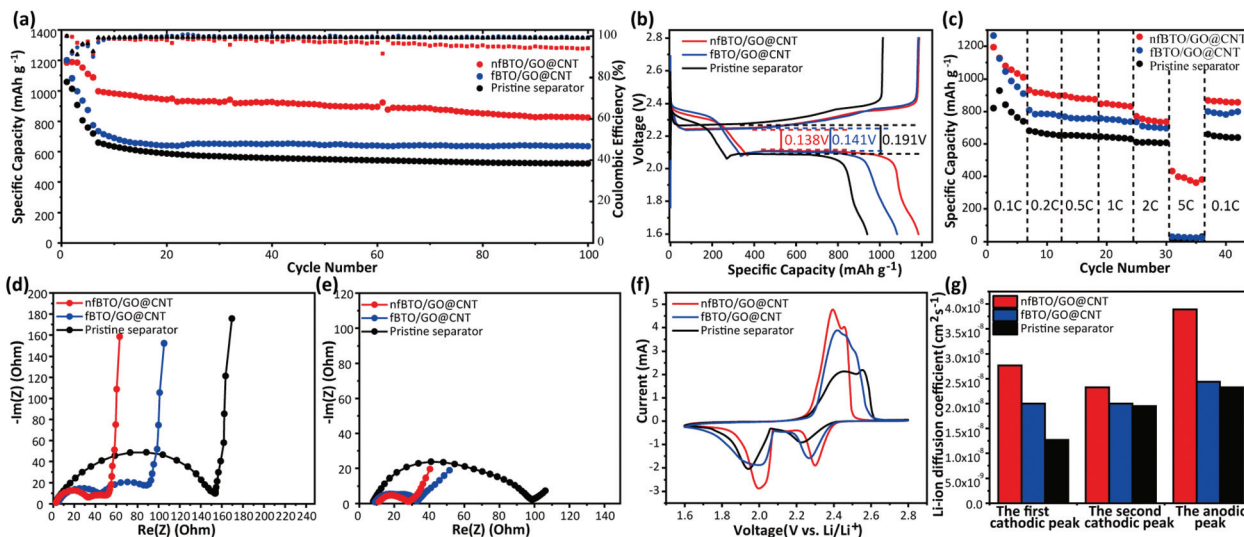
Fig. 2 Electrochemical performances of electrodes with an nfBTO/GO@CNT layer, an fBTO/GO@CNT layer, and a pristine separator. (a) Cycling performance; (b) charge–discharge curves; (c) rate performances; EIS results of (d) the fresh cells and (e) the cells after 100 cycles at 0.2 C; (f) CV profiles at a scan rate of 0.1 mV s^{-1}; (g) the Li-ion diffusion coefficients.

electrodes are shown in Fig. 2a. The electrode with the ultrathin nfBTO/GO@CNT functional layer showed the best cycle performance. It achieved an initial capacity of 1187.8 mA h g^{-1} at 0.1 C and maintained 824.5 mA h g^{-1} after 100 cycles at 0.2 C with a capacity retention of 69.4%. The electrode with the fBTO/GO@CNT layer delivered an initial capacity of 1200.4 mA h g^{-1} at 0.1 C. After 100 cycles at 0.2 C, the specific capacity decreased to 635.7 mA h g^{-1}, showing capacity retention of 53.0%. The electrode with the pristine separator displayed an initial capacity of 1059.2 mA h g^{-1} and underwent severe capacity fading, ending up with a low discharge capacity of 521.9 mA h g^{-1} and a low capacity retention of 49.3% after 100 cycles. The charge–discharge curves in the 2nd cycle of the electrodes with the three different separators/layers are shown in Fig. 2b. The upper and lower discharge plateaus correspond to the redox reactions from elemental S_8 to Li_2S_n ($4 \leq n \leq 8$) at 2.3 V and Li_2S_n ($1 \leq n \leq 4$) at 2.1 V. The voltage hysteresis values between the discharge and charge plateaus (ΔE) of the electrodes with the pristine separator and the fBTO/GO@CNT layer were approximately 0.191 V and 0.141 V, respectively. The ΔE value further decreased to 0.138 V after introducing the nfBTO/GO@CNT layer. The charge–discharge curves in the 10th, 50th, and 100th cycles of the electrodes with the nfBTO/GO@CNT layer, fBTO/GO@CNT layer, and pristine separator are shown in Fig S3.† The electrodes with the nfBTO/GO@CNT layer showed the lowest ΔE values, being 0.150, 0.152, and 0.168 V in the 10th, 50th, and 100th cycles, respectively. In general, low voltage hysteresis represents high reversibility and fast redox kinetics of the cells. The lowest ΔE value suggested that the GO sheets and CNT films can facilitate ion transfer during the electrochemical reactions,[45] and the nfBTO nanoparticles can also accelerate the polysulfide conversion activity in the electrode with the nfBTO/GO@CNT functional layer. Moreover, the GO sheets and CNT films served as a current collector and provided abundant path-

ways for ion transfer during the chemical interaction between BTO nanoparticles and polysulfides.

The rate performances of the CNT@S electrodes are shown in Fig. 2c. The electrode with the nfBTO/GO@CNT functional layer delivered specific capacities of 1194, 932.3, 897.9, 847.1, 770.1, and 432.7 mA h g^{-1} at 0.1 C, 0.2 C, 0.5 C, 1 C, 2 C, and 5 C, respectively. In contrast, lower capacity values at 0.1–2 C and capacity collapse at 5 C were observed for cells with the pristine separator and the fBTO/GO@CNT layer. After the cycling rate decreased to 0.1 C, the electrode with the nfBTO/GO@CNT functional layer exhibited a capacity of 867.9 mA h g^{-1}, higher than the capacities of the electrodes with the fBTO/GO@CNT layer (799.9 mA h g^{-1}) and the pristine separator (659.7 mA h g^{-1}). The electrode with the nfBTO/GO@CNT functional layer showed better rate performance and higher reversible capability, suggesting the effect of the nfBTO/GO@CNT functional layer on trapping polysulfides and improving the redox reaction kinetics.

The cycling performance of the electrode with the nfBTO/GO@CNT interlayer at 0.1 C for three times and then at 1 C is shown in Fig. S4a†; the sulfur loading of the CNT@S electrode was 1.11 mg cm^{-2}. The cell showed an initial capacity of 1040.6 mA h g^{-1} at 1 C and 859.6 mA h g^{-1} after 200 cycles with a capacity retention of 82.6%, and the decay rate was 0.088% per cycle. Furthermore, high sulfur loading (5.49 mg cm^{-2}) CNT@S electrodes with the nfBTO/GO@CNT functional layer were tested (Fig. S4b†). The cell cycled five times at 0.1 C and 0.2 C afterward. The cell with the nfBTO/GO@CNT functional layer showed an initial discharge capacity of 937.4 mA h g^{-1} at 0.1 C, equivalent to an areal capacity of 5.15 mA h cm^{-2}, and the cell delivered 624.7 mA h g^{-1} after 100 cycles at 0.2 C. The cycle performances of the electrodes with the nfBTO/GO@CNT interlayer are compared with the data in the literature that applied functional interlayers in Li–S batteries

(Table S1†).[31,32,46–49] The electrodes in this work had a higher sulfur loading and showed higher areal capacity.

EIS tests were used to investigate the effect of the nfBTO/GO@CNT functional layer on the electrochemical kinetics of Li–S batteries. The Nyquist plots were constructed for the electrodes at frequencies from 100 MHz to 100 kHz. The semicircles at high frequency represented the charge transfer resistance of polysulfides. The semicircles at middle frequency were linked with the dissolution of S_8 and the formation of Li_2S and Li_2S_2. The line at low frequency was associated with inner diffusion.[50] The equivalent circuit is shown in Fig. S5a.† R_0 is the interphase-contact resistance of the electrolyte and electrode, and R_1 and R_2 correspond to the semicircles at high frequency and middle frequency, respectively. Before cycling, the electrodes with the nfBTO/GO@CNT and fBTO/GO@CNT layers showed resistances of 30.32 Ω and 42.08 Ω at the high frequency and 17.25 Ω and 28.06 Ω at the middle frequency (Fig. 2d), respectively. The resistance of the electrode with the pristine separator was 144.5 Ω. After 100 cycles at 0.2 C, the electrode with the nfBTO/GO@CNT functional layer still exhibited the lowest resistance (12.4 Ω and 8.542 Ω) among the electrodes with different separator/layers (Fig. 2e and S5b†). The smaller resistance of the cell with the nfBTO/GO@CNT functional layer indicates faster charge transfer behavior, suggesting enhanced reaction kinetics and polysulfide conversion reversibility due to the introduction of the nfBTO/GO@CNT functional layer.

CV tests were performed to further study the electrochemical performances of the electrodes with the pristine separator and the nfBTO/GO@CNT and fBTO/GO@CNT layers (Fig. 2f), and the scanning rate was 0.1 mV s⁻¹. Two sharp cathodic peaks at 2.3 V and 2.0 V (*vs.* Li/Li⁺) were associated with the stepwise reduction of sulfur to soluble intermediate lithium polysulfides and the insoluble final reaction product Li_2S, respectively. Anodic peaks were observed at 2.4 V. The electrode with the nfBTO/GO@CNT functional layer showed sharper redox peaks than those with the pristine separator and the fBTO/GO@CNT layer, indicating improved electrochemical reaction kinetics by the synergetic effect of the nfBTO nanoparticles, GO sheets, and CNT films. CV measurements were also conducted at various scan rates from 0.1 mV s⁻¹ to 0.5 mV s⁻¹ to investigate the ion transfer kinetics in the electrodes (Fig. S6a–c†). All the peak currents were linear with the square root of scanning rates, and the lithium-ion diffusion process was described by the Randles–Sevcik equation:[51]

$$I_P = (2.69 \times 10^5)n^{1.5}AD^{0.5}\nu^{0.5}C$$

In this work, the peak current (I_p) and the lithium-ion diffusion coefficient (D) were variables, the charge transfer number n was 2, the area of the active electrode A was 0.785 cm², the concentration of Li ions (C) was 1 mol cm⁻¹, and the scan rates (ν) ranged from 0.1 to 0.5 mV s⁻¹. Therefore, the slope of the plot was correlated to lithium-ion diffusion. Fig. 2g shows that for the electrode with the nfBTO/GO@CNT functional layer, the Li-ion diffusion coefficient (D)

values derived from the slopes at different cathodic/anodic peaks were 2.77×10^{-8}, 2.30×10^{-8}, and 3.89×10^{-8} cm² s⁻¹, respectively, which were higher than those of the electrodes with the fBTO/GO@CNT layer (2.00×10^{-8}, 2.00×10^{-8}, and 2.44×10^{-8} cm² s⁻¹) and the pristine separator (1.27×10^{-8}, 1.95×10^{-8}, and 2.33×10^{-8} cm² s⁻¹). The higher Li-ion diffusion coefficient in the electrode with the nfBTO/GO@CNT functional layer suggests that Li-ions can pass through the nfBTO/GO@CNT layer more easily, consistent with the results of the EIS tests that showed smaller resistance. These results indicated that the GO sheets and CNT films with high conductivity facilitated electron and ion transfer. Furthermore, the higher Li-ion diffusion coefficient suggested that the nfBTO nanoparticles have stronger adsorption of polysulfides than the fBTO nanoparticles and further accelerate the redox kinetics of polysulfide conversion in the electrode with the nfBTO/GO@CNT functional layer.[46,52]

The polysulfide trapping abilities of different functional layers were investigated using H-type glass bottles (Fig. 3a). The Li_2S_4 solution and DOL/DME solvent were in the left and right bottles, respectively. Li_2S_4 tends to diffuse from the left bottle to the right bottle due to the concentration gradient. The pristine separator and the nfBTO/GO@CNT and fBTO/GO@CNT layers were put between the two bottles to prevent the diffusion of Li_2S_4. The DOL/DME solvent in the right bottles with the pristine separator and the fBTO/GO@CNT layer turned from colorless to yellow and light yellow after 3 h, respectively, indicating their poor capabilities in suppressing the polysulfide diffusion. By contrast, the DOL/DME solvent with the nfBTO/GO@CNT layer showed little color change after 9 h, demonstrating the better ability of the nfBTO/GO@CNT layer in trapping polysulfides. Furthermore, the ability of BTO particles to adsorb polysulfides was investigated (Fig. 3b). The inset photograph in Fig. 3b shows that the Li_2S_4 solution became almost colorless after adding nfBTO particles, and the color of the Li_2S_4 solution showed little change after adding fBTO particles. The concentration changes of Li_2S_4 in the supernatant were further detected by UV-vis spectroscopy. Among the Li_2S_4, $fBTO/Li_2S_4$, and $nfBTO/Li_2S_4$ solutions, the intensity of the absorption peak of the $nfBTO/Li_2S_4$ solution was the lowest, demonstrating the strongest polysulfide adsorbance capability of the nfBTO nanoparticles.

XPS analysis of the fBTO and nfBTO nanoparticles before and after treating with Li_2S_4 solution was performed to study the chemical interaction between the BTO nanoparticles and polysulfides. For the nfBTO nanoparticles, the spectra in Fig. 4a show the original Ba 3d³ and 3d⁵ peaks at 796.31 eV, 795.42 eV, 780.96 eV and 779.98 eV, which moved to 795.54 eV, 794.81 eV, 780.15 eV and 779.41 eV, respectively, after Li_2S_4 treatment. For the fBTO nanoparticles, the Ba 3d³ and Ba 3d⁵ peaks showed small changes before and after Li_2S_4 treatment (Fig. 4b). The change in the binding energies of Ba 3d³ and Ba 3d⁵ after soaking nfBTO nanoparticles in Li_2S_4 solution suggested the presence of chemical bonding between Ba and S, resulting in the efficient trapping of polysulfides by the nfBTO nanoparticles in the functional layer.
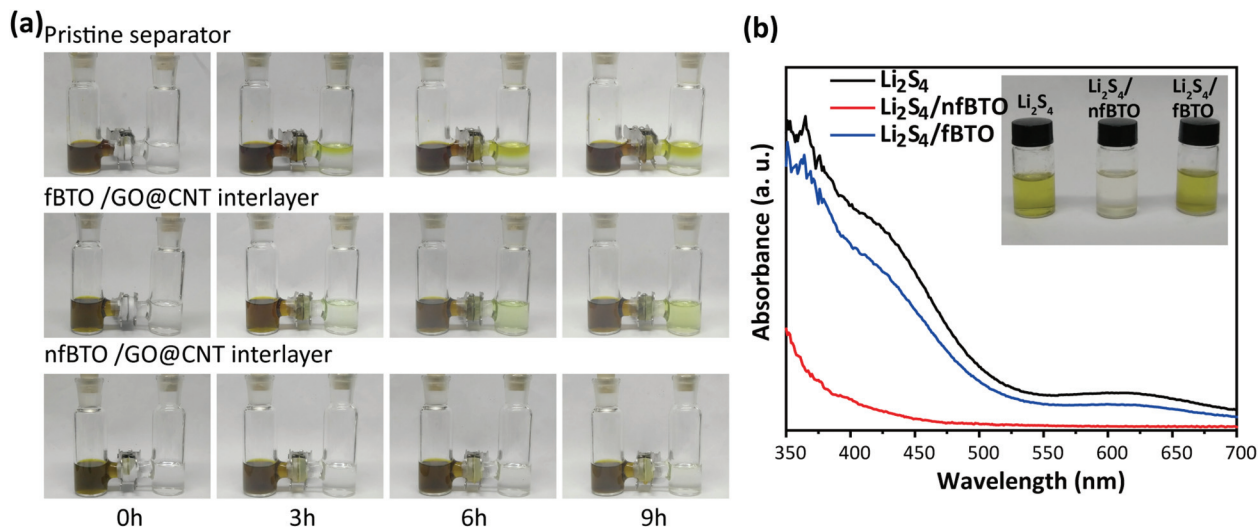
Fig. 3 (a) Photographs of H-type glass bottles with Li_2S_4 solution in the left bottles and the DOL/DME solvent in the right bottles, separated by a pristine separator (top row), an fBTO/GO@CNT layer coated separator (middle row), and an nfBTO/GO@CNT layer coated separator (bottom row); (b) UV-vis spectra of the supernatant of Li_2S_4, Li_2S_4/nfBTO, and Li_2S_4/fBTO solutions. Inset: Photograph of the polysulfide adsorption by nfBTO and fBTO nanoparticles.
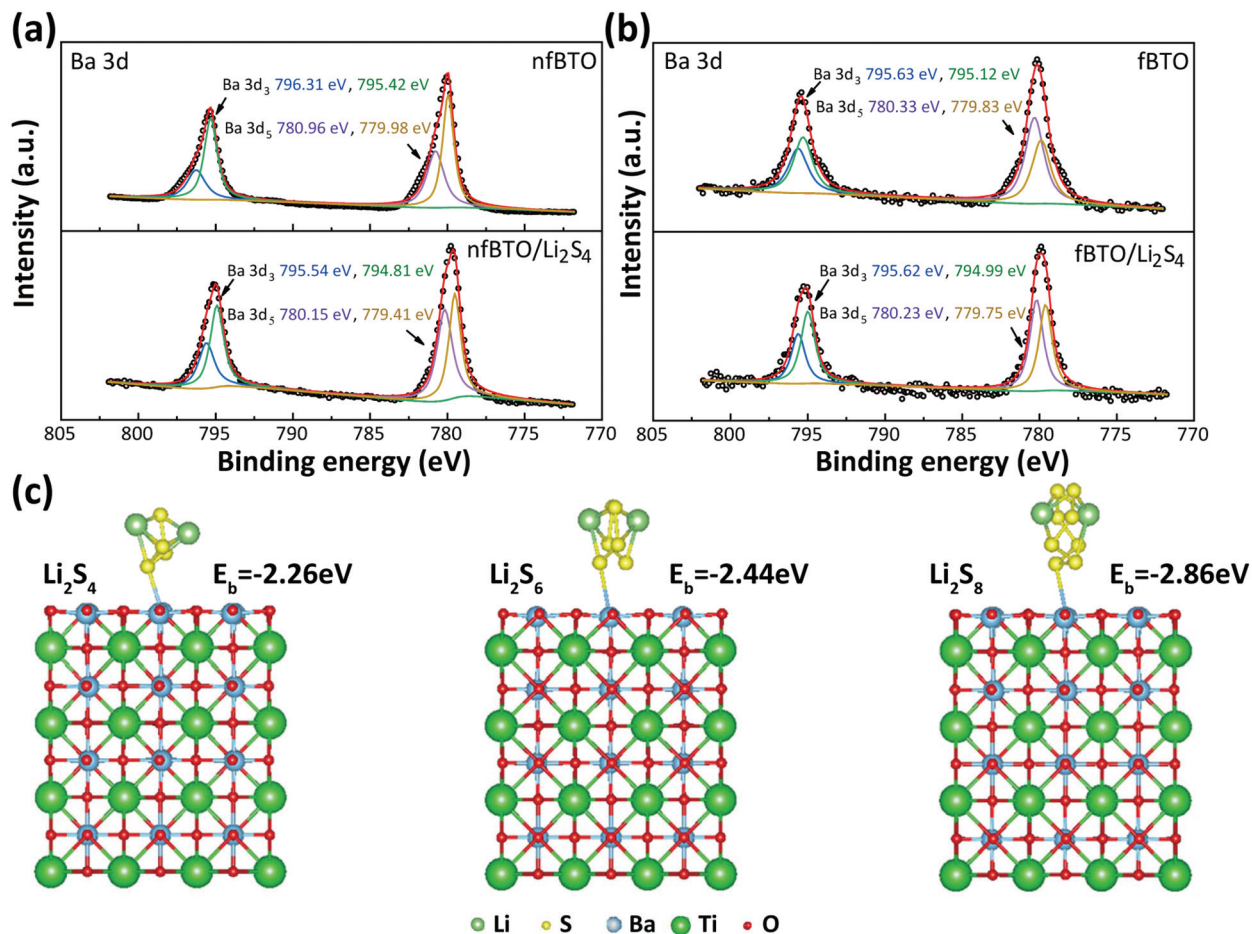

Fig. 4 XPS spectra of BTO before and after treating (a) nfBTO nanoparticles and (b) fBTO nanoparticles with Li_2S_4. (c) Binding geometries and DFT calculation of binding energies of nfBTO with Li_2S_n.
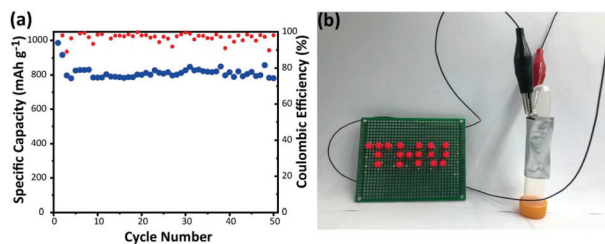
Fig. 5 (a) Cycling performance of a pouch cell with an nfBTO/GO@CNT functional layer at 0.05 C. (b) Photograph of an illuminated LED array powered by a pouch cell in a bent condition.

To further understand the adsorptive behavior of the BTO/GO@CNT layer, first-principles DFT simulations were employed. As shown in Fig. 4c and S7,† the primary chemical bonding between the BTO nanoparticles and polysulfides is Ba–S. The binding energies (E_b) between nfBTO and polysulfides (Li_2S_n, n = 2, 6, and 8) were −2.26 eV, −2.44 eV, and −2.86 eV, respectively. With the increase of n in Li_2S_n, more active sites appeared on the polysulfides, and the absolute value of E_b showed an upward trend. The absolute values of E_b between fBTO and Li_2S_n were relatively smaller (−2.23 eV, −2.35 eV, and −2.71 eV). This finding matches the adsorption and trapping experiments and confirms the superior ability of nfBTO nanoparticles in trapping polysulfides and alleviating the shuttle effect.

The photographs and SEM images of the fBTO/GO@CNT and nfBTO/GO@CNT layers after 50 cycles at 0.2 C are shown in Fig. S8.† In both samples, the BTO/GO@CNT layers were attached to the separator, and the cross-stacked CNT films in the BTO/GO@CNT layers remained intact after cycling. These results suggest that the BTO/GO@CNT layers demonstrated structural stability during cycling.

The excellent electrochemical performances of sulfur electrodes with the nfBTO/GO@CNT functional layer suggest the potential of the nfBTO/GO@CNT functional layer in developing high-performance Li–S batteries. Pouch cells with the nfBTO/GO@CNT functional layer were also assembled to explore the possibility in practical applications. As shown in Fig. 5a, the Li–S pouch cell achieved an initial capacity of 985.3 mA h g^{-1}, and its capacity decreased to 780.7 mA h g^{-1} after 50 cycles at 0.05 C. The capacity retention was 79.2%, and the coulombic efficiency remained at 98.06%. A pouch cell was bent around a glass tube and lighted an LED array with a "THU" pattern, demonstrating its excellent flexibility (Fig. 5b). The pouch cell's stable electrochemical performance suggests that the nfBTO/GO@CNT layer can serve as a functional, protective separator for practical Li–S cells.

Conclusions

An ultrathin and flexible BTO/GO@CNT layer is introduced between the sulfur electrode and separator to improve the electrochemical performance of the Li–S battery. Both nfBTO

nanoparticles and fBTO nanoparticles are applied. The electrode with the nfBTO/GO@CNT functional layer delivers a higher initial capacity of 1187.8 mA h g^{-1} at 0.1 C. Electrodes with a high sulfur loading of 5.49 mg cm^{-2} with the functional layer exhibit an areal capacity of 5.15 mA h cm^{-2} at 0.1 C. The pouch cell with the nfBTO/GO@CNT functional layer exhibits an initial capacity of 985.3 mA h g^{-1} at 0.05 C and excellent flexibility. The results of adsorption/trapping experiments and DFT calculations suggest that nfBTO nanoparticles can trap and interact with polysulfides more effectively by chemical bonding than fBTO nanoparticles. The introduction of nfBTO nanoparticles provides many sites for the adsorption of polysulfides, promotes the conversion of polysulfides, and accelerates the redox kinetics in the electrode. Furthermore, the cross-stacked CNT films and GO sheets serve as a porous current collector, promoting electron and ion transfer and accelerating redox reaction kinetics. Therefore, the nfBTO/GO@CNT functional layer effectively mitigates the diffusion of polysulfides and improves the electrochemical performances, providing a feasible strategy to produce high-performance Li–S batteries.

Conflicts of interest

There are no conflicts to declare.

Acknowledgements

Notes and references

1 X. Ji, K. T. Lee and L. F. Nazar, *Nat. Mater.*, 2009, **8**, 500–506.
2 P. G. Bruce, S. A. Freunberger, L. J. Hardwick and J.-M. Tarascon, *Nat. Mater.*, 2012, **11**, 172.
3 A. Manthiram, Y. Fu, S.-H. Chung, C. Zu and Y.-S. Su, *Chem. Rev.*, 2014, **114**(23), 11751–1178787.
4 A. Rosenman, E. Markevich, G. Salitra, D. Aurbach, A. Garsuch and F. F. Chesneau, *Adv. Energy Mater.*, 2015, **5**(16), 1500212.
5 G. Zhou, S. Pei, L. Li, D.-W. Wang, S. Wang, K. Huang, L.-C. Yin, F. Li and H.-M. Cheng, *Adv. Mater.*, 2014, **26**(4), 625–631.
6 G. Zhou, E. Paek, G. S. Hwang and A. Manthiram, *Nat. Commun.*, 2015, **6**, 7760.
7 W. Kong, L. Sun, Y. Wu, K. L. Jiang, Q. Q. Li, J. P. Wang and S. S. Fan, *Carbon*, 2016, **96**, 1053–1059.
8 L. Sun, M. Y. Li, Y. Jiang, W. B. Kong, K. L. Jiang, J. P. Wang and S. S. Fan, *Nano Lett.*, 2014, **14**, 4044–4049.

9 L. Sun, W. Kong, Y. Jiang, H. Wu, K. Jiang, J. Wang and S. Fan, *J. Mater. Chem. A*, 2015, **3**, 5305–5312.

10 C. Zhou, Q. He, Z. Li, J. Meng, X. Hong, Y. Li, Y. Zhao, X. Xu and L. Mai, *Chem. Eng. J.*, 2020, **395**, 124979.

11 J. Cao, C. Chen, Q. Zhao, N. Zhang, Q. Lu, X. Wang, Z. Niu and J. Chen, *Adv. Mater.*, 2016, **28**, 9629–9636.

12 L. Zhang, D. Liu, Z. Muhammad, F. Wan, W. Xie, Y. Wang, L. Song, Z. Niu and J. Chen, *Adv. Mater.*, 2019, **31**, 1903955.

13 J.-G. Wang, K. Xie and B. Wei, *Nano Energy*, 2015, **15**, 413–444.

14 H.-J. Peng and Q. Zhang, *Angew. Chem., Int. Ed.*, 2015, **54**(38), 11018–11020.

15 X. Liang, C. Hart, Q. Pang, A. Garsuch, T. Weiss and L. F. Nazar, *Nat. Commun.*, 2015, **6**, 5682.

16 Y. Tao, Y. Wei, Y. Liu, J. Wang, W. Qiao, L. Ling and D. Long, *Energy Environ. Sci.*, 2016, **9**, 3230–3239.

17 L. Hu, C. Dai, H. Liu, Y. Li, B. Shen, Y. Chen, S.-J. Bao and M. Xu, *Adv. Energy Mater.*, 2018, **8**(23), 1800709.

18 L. Kong, X. Chen, B.-Q. Li, H.-J. Peng, J.-Q. Huang, J. Xie and Q. Zhang, *Adv. Mater.*, 2017, **30**(2), 1705219.

19 Z. Li, C. Zhou, J. Hua, X. Hon, C. Sun, H.-W. Li, X. Xu and L. Mai, *Adv. Mater.*, 2020, **32**, 1907444.

20 H. Lin, L. Yang, X. Jiang, G. Li, T. Zhang, Q. Yao, G. W. Zheng and J. Y. Lee, *Energy Environ. Sci.*, 2017, **10**, 1476–1486.

21 Z. Yuan, H.-J. Peng, T.-Z. Hou, J.-Q. Huang, C.-M. Chen, D.-W. Wang, X.-B. Cheng, F. Wei and Q. Zhang, *Nano Lett.*, 2016, **16**(1), 519–527.

22 J. Park, B.-C. Yu, J. S. Park, J. W. Choi, C. Kim, Y.-E. Sung and J. B. Goodenough, *Adv. Energy Mater.*, 2017, **7**(11), 1602567.

23 Z. Cui, C. Zu, W. Zhou, A. Manthiram and J. B. Goodenough, *Adv. Mater.*, 2016, **28**(22), 6926–6931.

24 Z. Sun, J. Zhang, L. Yin, G. Hu, R. Fang, H.-M. Cheng and F. Li, *Nat. Commun.*, 2017, **8**, 14627.

25 L. Zhang, X. Chen, F. Wan, Z. Niu, Y. Wang, Q. Zhang and J. Chen, *ACS Nano*, 2018, **12**, 9578–9586.

26 Y. Zhong, L. Yin, P. He, W. Liu, Z. Wu and H. Wang, *J. Am. Chem. Soc.*, 2018, **140**, 1455–1459.

27 J. Cheng, D. Zhao, L. Fan, X. Wu, M. Wang, N. Zhang and K. Sun, *J. Mater. Chem. A*, 2017, **5**, 14519–14524.

28 T. Zhou, Y. Zhao, G. Zhou, W. Lv, P. Sun, F. Kang, B. Li and Q.-H. Yang, *Nano Energy*, 2017, **39**, 291–296.

29 H.-J. Peng, G. Zhang, X. Chen, Z.-W. Zhang, W.-T. Xu, J.-Q. Huang and Q. Zhang, *Angew. Chem., Int. Ed.*, 2016, **55**(42), 12990–12995.

30 K. Xie, Y. You, K. Yuan, W. Lu, K. Zhang, F. Xu, M. Ye, S. Ke, C. Shen, X. Zeng, X. Fan and B. Wei, *Adv. Mater.*, 2017, **29**(6), 1604724.

31 T. Yim, S. H. Han, N. H. Park, M.-S. Park, J. H. Lee, J. Shin, J. W. Choi, Y. Jung, Y. N. Jo, J.-S. Yu and K. J. Kim, *Adv. Funct. Mater.*, 2016, **26**(43), 7817–7823.

32 S. Zhang, X. Qin, Y. Liu, L. Zhang, D. Liu, Y. Xia, H. Zhu, B. Li and F. Kang, *Adv. Mater. Interfaces*, 2019, **6**(22), 1900984.

33 Z. Zhao, G. Li, Z. Wang, M. Feng, M. Sun, X. Xue, R. Liu, H. Jia, Z. Wang, W. Zhang, H. Li and Z. Chen, *J. Power Sources*, 2019, **434**, 226729.

34 K. Jiang, Q. Li and S. Fan, *Nature*, 2002, **419**, 801.

35 K. Liu, Y. Sun, L. Chen, C. Feng, X. Feng, K. Jiang, Y. Zhao and S. Fan, *Nano Lett.*, 2008, **8**(2), 700–705.

36 K. Liu, K. Jiang, Y. Wei, S. Ge, P. Liu and S. Fan, *Adv. Mater.*, 2007, **19**(7), 975–978.

37 X. B. Zhang, K. L. Jiang, C. Feng, P. Liu, L. Zhang, J. Kong, T. H. Zhang, Q. Q. Li and S. S. Fan, *Adv. Mater.*, 2006, **18**, 1505.

38 K. L. Jiang, J. P. Wang, Q. Q. Li, L. A. Liu, C. H. Liu and S. S. Fan, *Adv. Mater.*, 2011, **23**, 1154.

39 K. Liu, Y. H. Sun, P. Liu, J. P. Wang, Q. Q. Li, S. S. Fan and K. L. Jiang, *Nanotechnology*, 2009, **20**, 335705.

40 J. P. Perdew, K. Burke and M. Ernzerhof, *Phys. Rev. Lett.*, 1996, **77**, 3865–3868.

41 P. E. Blöchl, *Phys. Rev. B: Condens. Matter Mater. Phys.*, 1994, **50**, 17953–17979.

42 G. Kresse and J. Furthmüller, *Phys. Rev. B: Condens. Matter Mater. Phys.*, 1996, **54**, 11169–11186.

43 S. Grimme, J. Antony, S. Ehrlich and H. Krieg, *J. Chem. Phys.*, 2010, **132**, 154104.

44 H. J. Monkhorst and J. D. Pack, *Phys. Rev. B: Solid State*, 1976, **13**, 5188–5192.

45 S.-H. Chung and A. Manthiram, *Adv. Funct. Mater.*, 2014, **24**(33), 5299–5306.

46 H. Yuan, H. Peng, B. Li, J. Xie, L. Kong, M. Zhao, X. Chen, J. Huang and Q. Zhang, *Adv. Energy Mater.*, 2019, **9**, 1802768.

47 P. Cheng, P. Guo, K. Sun, Y. Zhao, D. Liu and D. He, *J. Membr. Sci.*, 2021, **619**, 118780.

48 S. Kong, D. Cai, G. Li, X. Xu, S. Zhou, X. Ding, Y. Zhang, S. Yang, X. Zhou, H. Nie, S. Huang, P. Peng and Z. Yang, *Nanoscale*, 2021, **13**, 3817–3826.

49 M. E. Pam, S. Huang, S. Fan, S. Geng, D. Kong, S. Chen, M. Ding, L. Guo, L. K. Ang and H. Y. Yang, *Mater. Today Energy*, 2020, **16**, 100380.

50 N. A. Cañas, K. Hirose, B. Pascucci, N. Wagner, K. A. Friedrich and R. Hiesgen, *Electrochim. Acta*, 2013, **97**, 42–51.

51 X. Tao, J. Wang, C. Liu, H. Wang, H. Yao, G. Zheng, Z. W. Seh, Q. Cai, W. Li, G. Zhou, C. Zu and Y. Cui, *Nat. Commun.*, 2016, **7**, 11203.

52 G. Zhou, H. Tian, Y. Jin, X. Tao, B. Liu, R. Zhang, Z. W. She, D. Zhuo, Y. Liu, J. Sun, J. Zhao, C. Zu, D. S. Wu, Q. Zhang and Y. Cui, *Proc. Natl. Acad. Sci. U. S. A.*, 2017, **114**(5), 840–845.

Electronic supplementary information

Efficient Polysulfide Trapping in Lithium-Sulfur Batteries Using Ultrathin and Flexible BaTiO₃/Graphene Oxide/Carbon Nanotube Layers

Jing Wangᵃ, Zhe Shiᵇ, Yufeng Luoᵃ, Datao Wangᵃ, Hengcai Wuᵃ, Qunqing Liᵃᶜ, Shoushan Fanᵃᶜ, Ju Liᵇ, and Jiaping Wang*ᵃᶜ

a. *Department of Physics and Tsinghua-Foxconn Nanotechnology Research Center, Tsinghua University, Beijing 100084, China. E-mail: jpwang@tsinghua.edu.cn.*

b. *Department of Nuclear Science and Engineering and Department of Materials Science and Engineering, Massachusetts Institute of Technology, Cambridge, MA 02139, USA.*

c. *Frontier Science Center for Quantum Information, Beijing 100084, China.*
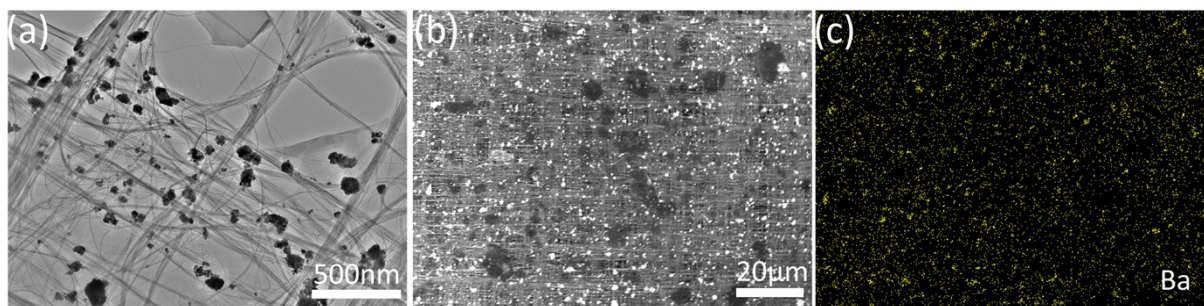
Fig. S1 (a) TEM and (b) SEM images of a fBTO/GO@CNT layer. (c) Ba elemental mapping of (b).
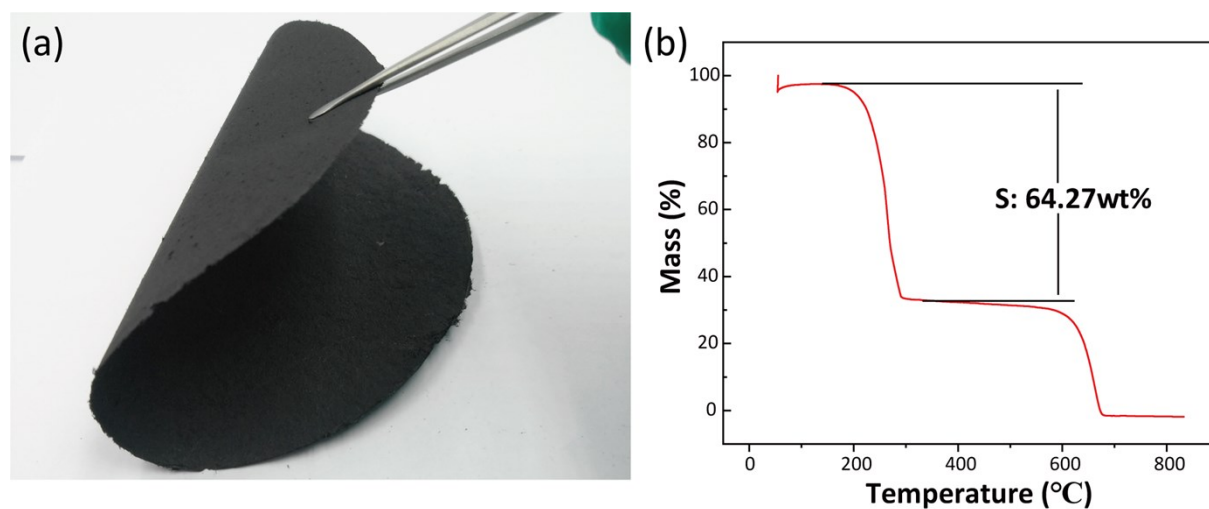

**Fig. S2** (a) Photograph and (b) TGA curve of a flexible CNT@S electrode
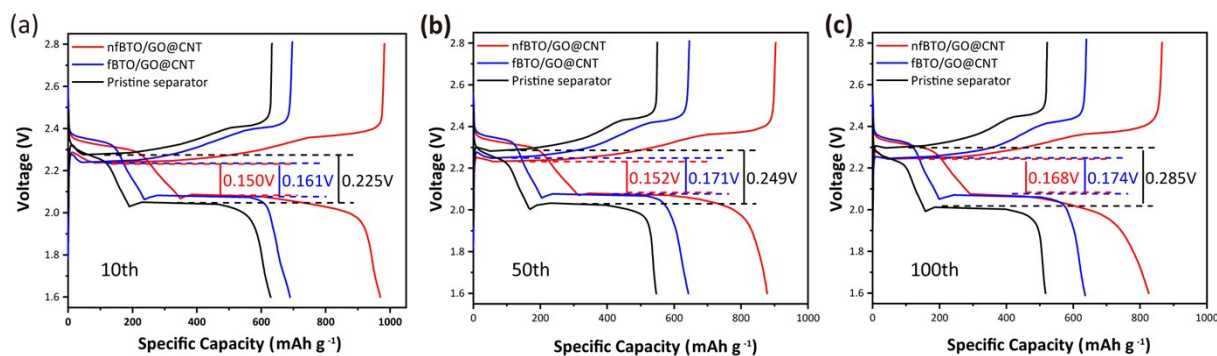
Fig. S3 Charge-discharge curves of the electrodes with the nfBTO/GO@CNT layer, fBTO/GO@CNT layer, and pristine separator in the (a) 10th, (b) 50th, and (c) 100th cycles.
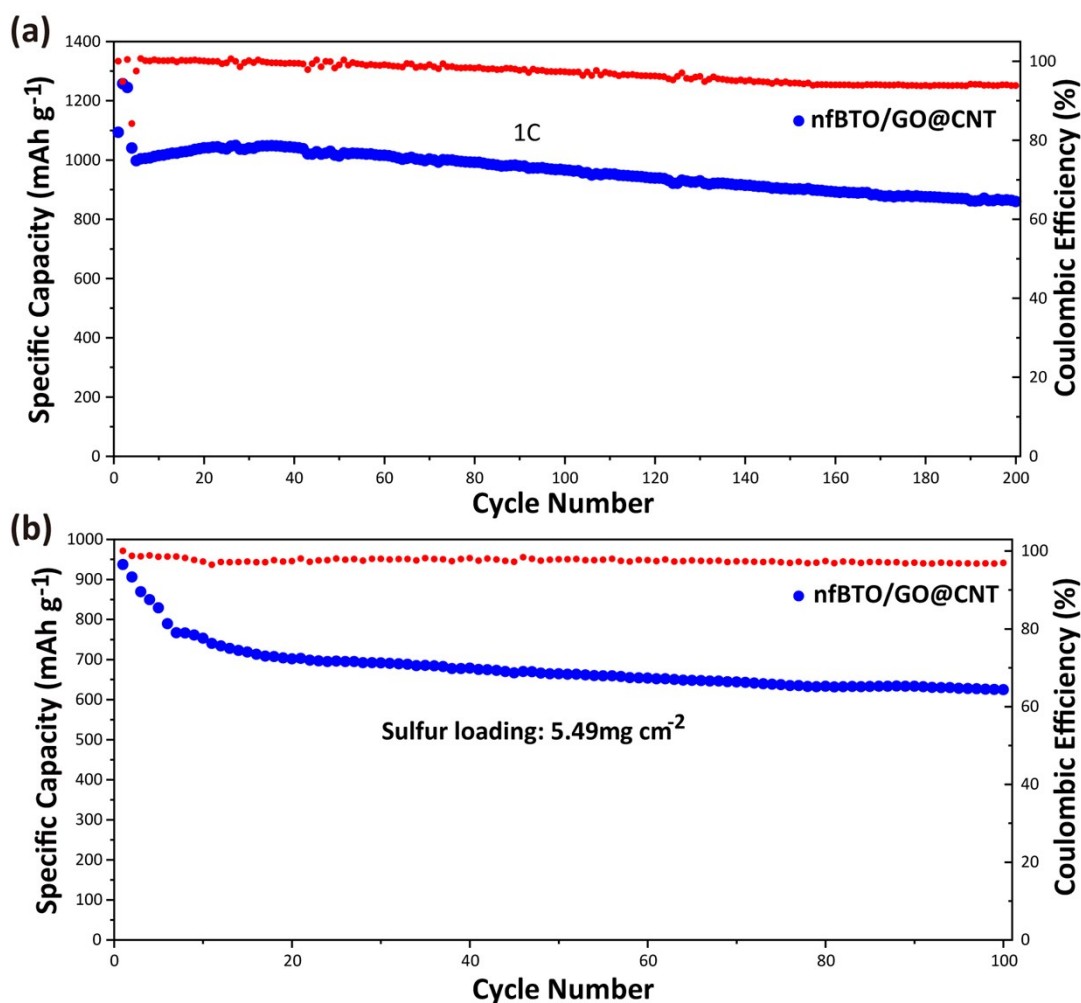

Fig. S4 Cycling performance of (a) an electrode with the nfBTO/GO@CNT functional layer at 1 C and (b) a high-sulfur loading electrode with the nfBTO/GO@CNT functional layer at 0.2 C.
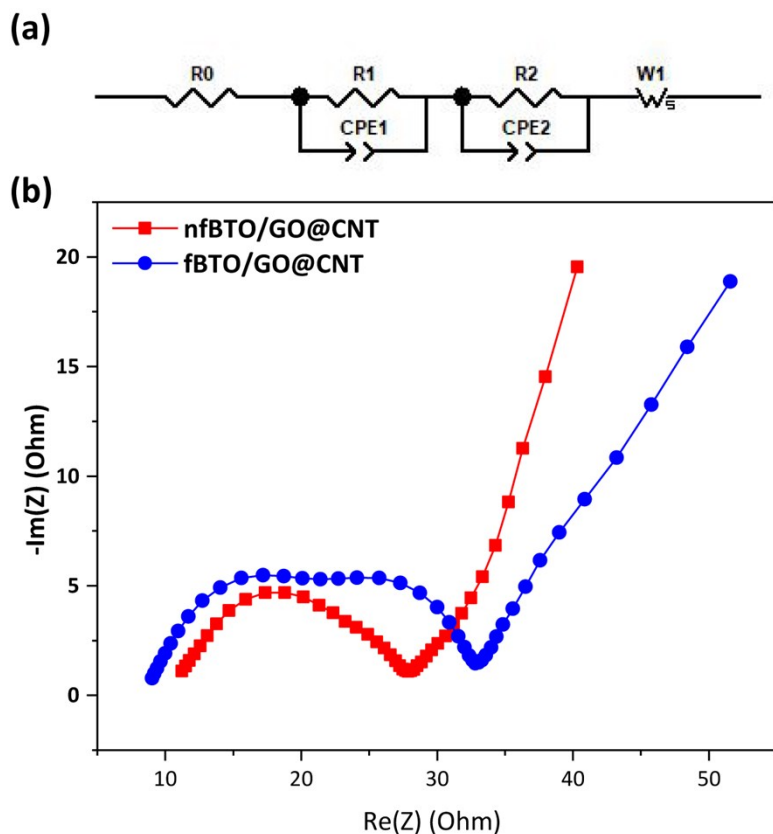
Fig. S5 (a) The equivalent circuit of the EIS tests. (b) The EIS rests of the cells with the nfBTO/GO@CNT and fBTO/GO@CNT layers after 100 cycles.
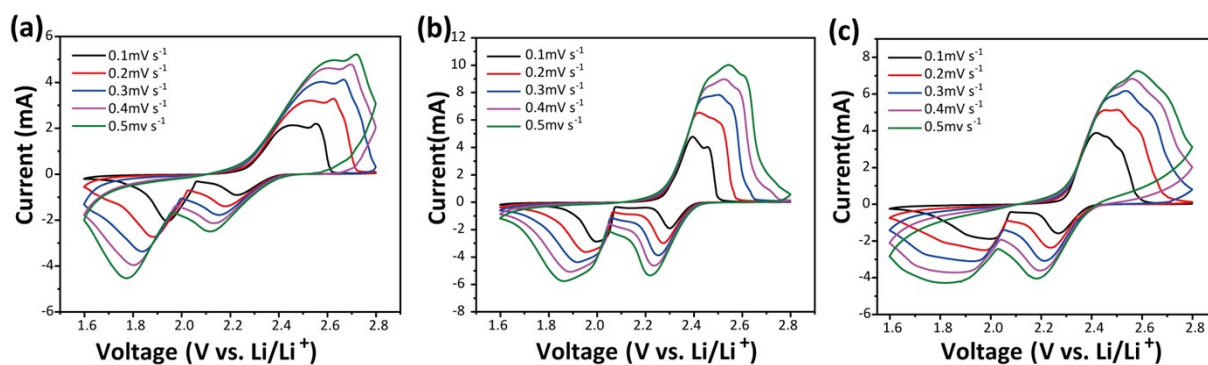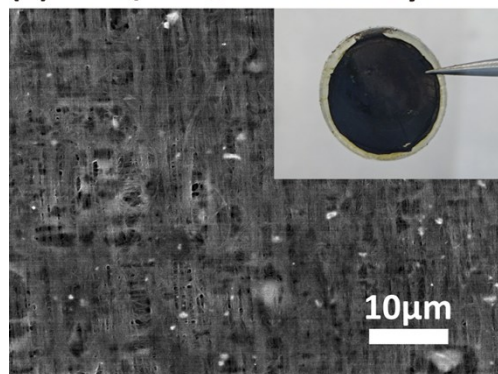

Fig. S6 CV profiles of electrodes with (a) a pristine separator, (b) an nfBTO/GO@CNT layer, and (c) a fBTO/GO@CNT layer at different scan rates
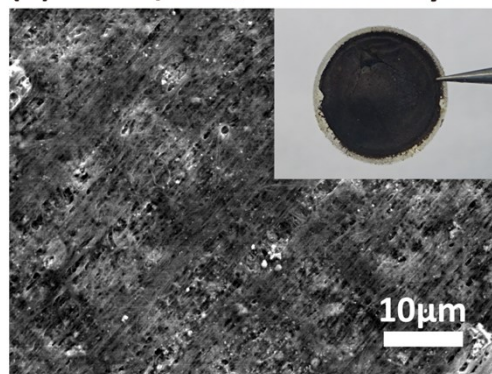
Li$_2$S$_4$ E$_b$=-2.23eV   Li$_2$S$_6$ E$_b$=-2.35eV   Li$_2$S$_8$ E$_b$=-2.71eV

○ Li   ● S   ○ Ba   ● Ti   ● O
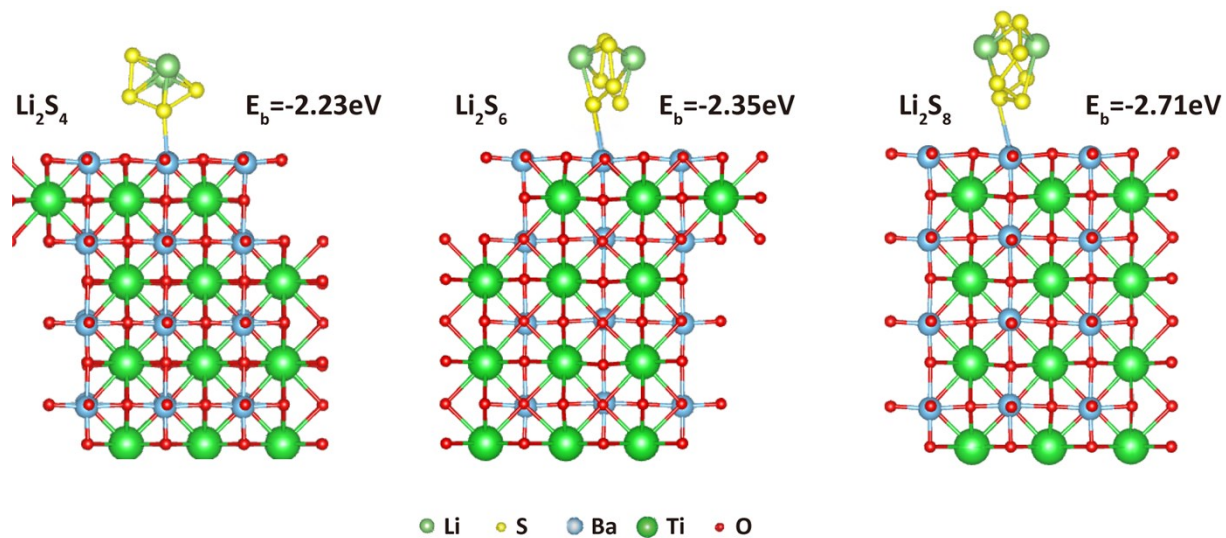
Fig. S7 Binding geometries and DFT calculation of binding energies of fBTO with Li$_2$S$_n$

(a) fBTO/GO@CNT interlayer   (b) nfBTO/GO@CNT interlayer

10µm   10µm

Fig. S8 Photographs and SEM images of (a) fBTO/GO@CNT and (b) nfBTO/GO@CNT layers after 50 cycles at 0.2 C.

Table S1 Comparison of cycle performances of the sulfur electrodes with nfBTO/GO@CNT layer and data in the literature

Functional interlayer	Sulfur loading (mg cm^{-2})	Rate (C)	Initial capacity (mAh g^{-1})	Areal capacity (mAh cm^{-2})	References
Dipole-aligned BTO coated separator	3	0.1	1122.1	3.37	[1]
rGO/BTO@CNF interlayer	4.616	0.1	917	4.23	[2]
CoSe$_2$/G functional separator	4.35	0.2	1098	4.78	[3]
CeO2@G modified separator	5.03	0.3	589	2.96	[4]
Gra-HsGDY	1.2	0.2	1267	1.52	[5]
WS@SS interlayer	2.4	0.1	1362	3.27	[6]
nfBTO/GO@CNT functional layer	5.49	0.1	937.4	5.15	This work

References

[1] T. Yim, S. H. Han, N. H. Park, M.-S. Park, J. H. Lee, J. Shin, J. W. Choi, Y. Jung, Y. N. Jo, J.-S. Yu, and K. J. Kim, *Adv. Funct. Mater.* 2016, **26**, 7817-7823.

[2] S. Zhang, X. Qin, Y. Liu, L. Zhang, D. Liu, Y. Xia, H. Zhu, B. Li, and F. Kang, *Adv. Mater. Interfaces* 2019, **6**, 22, 1900984.

[3] H. Yuan, H. Peng, B. Li, J. Xie, L. Kong, M. Zhao, X. Chen, J. Huang, and Q. Zhang, *Adv. Energy Mater.* 2019, **9**, 1802768.

[4] P. Cheng, P. Guo, K. Sun, Y. Zhao, D. Liu, and D. He, *J. Mmebrane Sci.* 2021, **619**, 118780.

[5] S. Kong, D. Cai, G. Li, X. Xu, S. Zhou, X. Ding, Y. Zhang, S. Yang, X. Zhou, H. Nie, S. Huang, P. Peng, and Z. Yang, *Nanoscale* 2021, **13**, 3817-3826.

[6] M. E. Pam, S. Huang, S. Fan, S. Geng, D. Kong, S. Chen, M. Ding, L. Guo, L. K. Ang, and H. Y. Yang, *Mater. Today Energy* 2020, **16**, 100380.